Ocean Engineering 286 (2023) 115635

Contents lists available at ScienceDirect

Ocean Engineering

journal homepage: www.elsevier.com/locate/oceaneng

Hydroelastic response of a flexible spar floating wind turbine: Numerical modelling and validation

Xiaoming Ran [a,*], Vincent Leroy [b], Erin E. Bachynski-Polić [a]

[a] Department of Marine Technology, Norwegian University of Science and Technology, Trondheim, 7491, Norway
[b] Nantes Université, École Centrale Nantes, CNRS, LHEEA, UMR 6598, F-44000 Nantes, France

ARTICLE INFO

Keywords:
Floating wind turbines
Hydroelasticity
Distributed potential flow model
Validation
Coupled numerical simulation

ABSTRACT

This study examines the hydroelastic response of a large floating wind turbine (FWT) through coupled numerical analysis. Four numerical models with different levels of complexity in the hydrodynamic and structural modelling were established for a scaled 10 MW elastic spar FWT using the engineering tool SIMA. Two of them model the platform as a flexible body with distributed wave loads based on either Morison's equation or based on potential flow theory combined with Morison-type drag. The two other models consider the platform as a rigid body. These models were calibrated and validated against experimental results from a series of characterization tests (hammer test and decay test) and tests in waves (regular and irregular). Results for motions, strains, and tower base fore-aft bending moment are compared. All models predict damped natural periods for rigid body motions close to the experimental results from decay tests (within 4%). Overall, the wave-frequency responses (motion, strain on the platform, and tower base bending moment) in all models agree well with the experimental results in regular waves and irregular waves. For the structural internal loads around the 1st bending mode natural frequency, the distributed potential flow model agrees well with the experiments, while a large overestimation is seen in the flexible model with Morison's equation.

1. Introduction

Floating wind turbines (FWTs) are a promising solution to harness the significant wind energy resource in deep sea areas. However, cost reductions are needed.

Nowadays, both industry and academia are working on designing larger floating wind turbines in an effort to lower the levelized cost of energy (LCOE). Recently published designs include the UMaine VolturnUS 15 MW semi-submersible FWT (Allen et al., 2020), 20 MW spar FWT (Silva de Souza and Bachynski-Polić, 2022), and two 25 MW semi-submersible FWTs (Abdelmoteleb et al., 2022). The increasing turbine size requires increasingly large platforms to support the wind turbines. Thus, combining the up-scaling of the platform and cost-effective design will lead to a future generation of FWTs composed of slender and less stiff structures.

The design of the platform relies on numerical simulations for an extensive number of wind, wave, and operational conditions using engineering tools. Numerous numerical simulation tools have been developed to investigate the dynamics of full-scale FWTs (Jonkman and Musial, 2010). These engineering tools typically consider the substructure to be a rigid body, which is believed to be accurate enough for numerical analysis of small floating wind turbines. However, for (very) large platforms, this rigid body assumption becomes questionable. Thus, accurate and validated design tools that can consider the substructure flexibility are needed. For example, a hybrid finite element–boundary element (FE-BE) method has been developed for hydroelastic analysis of a very large floating structure (VLFS) with modular wave energy converters (WEC) (Cheng et al., 2022).

For floating wind turbines, several numerical developments and analyses including structural deformations have been presented in the literature. Beam theory is widely applied to model the floater when considering hull flexibility in time-domain analysis. Typically, the hydrodynamic loads used in engineering tools can be calculated using potential flow theory or Morison's equation, depending on the floating platform characteristics. When Morison's equation is adopted to determine the hydrodynamic loads, it is possible to calculate the internal loads of the platform directly in time-domain simulations using some existing numerical tools. For example, Karimirad and Moan (2010, 2011) and Campos et al. (2017) modelled spar platforms with beam elements and utilized Morison's equation to obtain global motions and internal loads of the platform. Thomsen et al. (2021) established flexible models for the TetraSpar floating wind turbine using Morison's equation. In most wave cases, the loads and moments in the structure

* Corresponding author.
E-mail address: xiaoming.ran@ntnu.no (X. Ran).

https://doi.org/10.1016/j.oceaneng.2023.115635
Received 12 June 2023; Received in revised form 11 July 2023; Accepted 13 August 2023
Available online 30 August 2023

increased when using the flexible models. However, Morison's equation is limited to slender bodies and is more suitable for simple geometries.

For large volume floating platforms, the potential flow force model is more suitable. Currently, in order to predict responses of the elastic floaters of FWTs efficiently, distributed hydrodynamic loads obtained from first-order potential flow theory based on the boundary element method (BEM) for a rigid body are usually used. With these methods, Silva de Souza and Bachynski (2020) observed that the hull elasticity changed the platform natural periods of a 5 MW TLP FWT significantly. In particular, the heave natural period increased by around 40%. The results also showed that pontoon flexibility resulted in amplified heave and pitch responses and higher tower base and tendon load responses.

In the case of semi-submersible FWTs, Luan et al. (2017a,b, 2018) investigated forces and moments in the floater of a 5 MW steel semi-submersible FWT. They used a multibody time-domain finite element model combined with potential flow theory. The change of mean floating position was found to lead to a different wetted surface and a considerable change in resulting sectional forces - even though the change in the resultant of the hydrodynamic pressure forces on the whole wetted body surface could be very limited (Luan et al., 2018). Although these studies considered a rigid hull, they gave insight into methods for obtaining internal loads using time domain simulations. Li et al. (2023) extended these works to account for flexibility in the column of the VolturnUS design, and found that flexibility has a significant influence on the global dynamic responses around the tower bending natural frequency. Recently, OpenFAST developed new functionality to include substructure flexibility in time domain simulations (Jonkman et al., 2020). Zhao et al. (2022) established coupled numerical models considering substructure flexibility using OpenFAST. They found that the substructure flexibility had a more significant impact on the fatigue damage of a 10 MW semi-submersible FWT in operating sea states than that in extreme sea states. However, the model that was used had some limitations. For example, cylindrical cross sections were used for modelling square-shaped beams. In the case of large size spar-type floating wind turbines, Silva de Souza and Bachynski-Polić (2022) modelled the platform as a flexible body and distributed wave loads from potential flow theory. Large extreme axial stresses were observed in the platform sections at still water level (SWL) and the Morison formulation over-predicted the fatigue damage significantly.

Numerical models considering substructure flexibility for FWTs in time domain simulations have not, however, been previously validated against model tests which include hull elasticity.

In the present work, four numerical models are established for the experimental spar FWT from the hydroelastic HELOFOW model tests (Leroy et al., 2022a,b). Two of the models consider elastic beam elements for the spar platform, while two consider a rigid platform. Both Morison's equation and potential flow theory are adopted for the hydrodynamic loads, which are distributed along the platform in the two fully-flexible models. All models are then calibrated and validated against the free decay tests and hammer tests, and responses in regular and irregular waves from experiments. The motion, elastic strain, and tower base fore-aft bending moment are examined.

The organization of this paper is as follows. In Section 2, the model tests are briefly described. Section 3 introduces the four numerical models. Next, the calibration and initial validation for the numerical models are presented in Section 4; the dynamic responses under a series of regular and irregular waves are analysed and discussed in Section 5; and conclusions are given in Section 6.

2. Experiment description

In the present work, the floating wind turbine is a 1/40 Froude-scaled spar-type floating wind turbine, which is used for experimental investigation of the hydroelastic response of a 10 MW spar FWT (Leroy et al., 2022a). The platform and tower of the experimental model are constructed with an elastic backbone, and the natural frequencies of the six rigid motions and first fore-aft bending mode are all Froude-scaled. A soft design was chosen for the purpose of accentuating the hydroelastic coupling and increasing the measurement accuracy, thus, the bending mode is more flexible than typical designs. The experimental campaign was performed at the Centrale Nantes Hydrodynamic and Ocean Engineering Tank, as shown in Fig. 1. All parameters, data and results are described in full scale except when explicitly mentioned.

Table 1
Spar platform main dimensions and inertia properties (full scale).

Item	Value	Unit
Platform length	94	m
Draft	90	m
Diameter below taper	18	m
Diameter above taper	11.2	m
Taper top below waterline	5.48	m
Taper length	8	m
Platform mass	1.88E+07	kg
Platform COG below waterline	71.6	m
Platform pitch inertia at COG	5.46E+09	$kg.m^2$

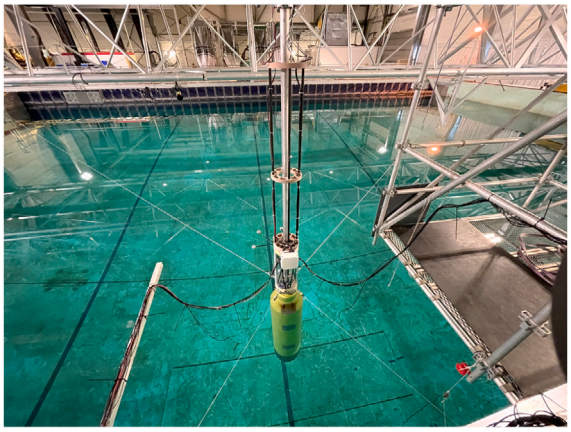

Fig. 1. Experimental model in the wave tank.

2.1. Test model

The spar platform, supporting the DTU 10 MW wind turbine, was designed by Centrale Nantes (Arnal, 2020). The main parameters of the platform are given in Table 1. The model is made of an inner backbone and six outer light floaters, which are mounted around the backbone. The backbone of the scaled model is made of aluminium 6060, with a mass density of 2700 kg/m^3 (model scale) and a Young's modulus of 69.5 GPa. The mast of the backbone has a diameter of 100 mm and a thickness of 5 mm (model scale). The light floaters, made of a composite foam, provide Froude-scaled buoyancy and hydrodynamic loads which are transmitted to the backbone. Clearance is ensured between the light floaters and between the floaters and the backbone so that the platform can bend freely.

The wind turbine, consisting of the tower and rotor-nacelle assembly (RNA), is mounted on top of the platform. The RNA is equipped with a fan to reproduce a constant thrust force. The properties of the wind turbine are given in Table 2. The RNA has the same targeted mass and centre of gravity as the DTU 10 MW turbine. The tower is made of the same aluminium as the platform backbone. The obtained frequency for the first global bending mode of the assembled model is 0.39 Hz.

A linear aerial mooring system is used for the tests, as shown in Fig. 2. The equilibrium model position in the absence of waves and wind is plotted in yellow. The right-handed coordinate system used here originates at the centre of the spar at the still water line, with

Table 2
Wind turbine properties.

Item	Value	Unit
Hub height	119	m
Height of WT COG w.r.t waterline	53.12	m
RNA mass	2.11E+06	kg
I_{yy} of the RNA around its COG	2.11E+09	kg.m^2

Table 3
Parameters of the mooring springs.

Item	Up-wave	Down-wave
Spring unstretched length (m)	39.2	24.0
Spring stiffness (N/m)	68800.0	37760.0
Line tension at equilibrium (N)	1.37E+06	1.19E+06

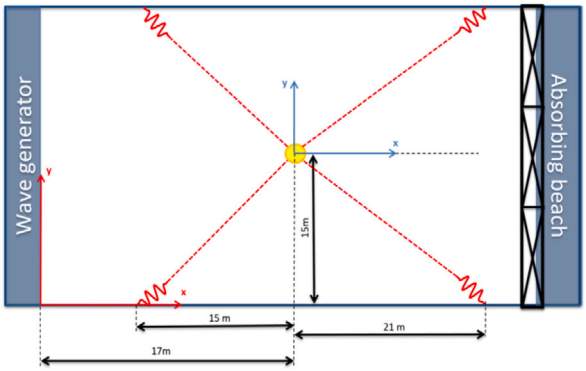

Fig. 2. Bird's eye view of the mooring layout (model scale).

positive x being in the direction of propagating waves, and z pointing upward. Each mooring line is made of an inextensible string and a spring installed on the wave tank wall. The string is attached to the mooring fairlead located at the spar top, 4 m above the waterline. Table 3 describes the parameters of the mooring spring, including the measured line pretension at the equilibrium position. The resulting global linear stiffness along the x and y-axes of this mooring system is measured to be 121.3 kN/m and 97.3 kN/m, respectively.

Several sensors are used to measure the response of the FWT model and the wave elevation. Wave gauges measure the wave elevation during both the wave calibration process and the model test campaign. The motion of the platform is measured using a Qualisys motion tracking system. The internal loads are measured at the transition piece (TP) located between the spar top and the tower using a 6 DOFs load cell. Strains are measured using strain gauges installed on the aluminium backbone of the platform. The strain gauges are placed at heights w.r.t waterline of: 0 m (strain 1), −16.52 m (strain 2), −31.56 m (strain 3).

2.2. Environmental conditions

The spar FWT has been studied in various environmental conditions, including regular waves and irregular waves. The tests were run both without and with a constant thrust on the nacelle. In the present work, only the cases without thrust are considered.

The regular waves are described in Table 4, with periods ranging from 4.9 to 19 s and wave steepnesses of 2%, 4% and 6%. Among these wave conditions, wave periods 5.20 s, 7.75 s and 10.33 s correspond to 2, 3 and 4 times the 1st fore-aft bending mode period, respectively. For wave conditions with these three wave periods, highly nonlinear responses were observed in the experiments (Leroy et al., 2022a).

The studied irregular sea states (SS) are presented in Table 5. Herein, the target significant wave heights H_s and peak periods T_p, inspired from the Gulf of Maine site (Gómez et al., 2015), are considered as medium severity environmental conditions and used for tests. The last three environmental conditions are the 5-year, 10-year and 50-year return period sea-states, respectively. For each irregular sea-state, the test lasts approximately 2 h in full scale.

Table 4
Measured calibrated regular waves for each wave period and steepness.

No.	T (s)	H-2% (m)	H-4% (m)	H-6% (m)
EC1	4.93	0.86	1.73	2.46
EC2	5.20	0.83	1.66	2.53
EC3	5.45	0.96	1.78	2.70
EC4	6.73	1.41	2.82	4.37
EC5	7.75	2.21	4.17	5.60
EC6	8.26	2.18	4.29	6.46
EC7	9.79	2.94	5.83	8.69
EC8	10.33	3.30	6.51	9.80
EC9	11.32	3.82	7.81	11.93
EC10	12.85	5.16	9.65	14.70
EC11	14.38	6.44	12.87	19.49
EC12	15.91	8.09	15.63	23.81
EC13	17.44	9.22	17.73	–
EC14	18.97	11.01	22.41	–

Table 5
Irregular sea states for the model tests.

No.	T_p (s)	H_s (m)
SS1	5	3
SS2	6	1.5
SS3	6.5	1.5
SS4	8	3
SS5	10	4
SS6	13.4	8.9
SS7	13.8	9.4
SS8	13.8	10.9

3. Numerical modelling

Numerical models of the model test are set up in the aero-hydro-servo-elastic engineering tool SIMA in full scale. The experimental model can be seen in Fig. 1. The four numerical models combining the rigid/flexible platform in the structural modelling and potential flow theory/Morison's equation for the wave load modelling are described in Table 6.

3.1. Structural modelling

As shown in Table 6, two different types of structural models are adopted for modelling the platform to investigate the effect of hull flexibility. The first one is named the rigid model, which treats the platform as a fully rigid body without deformation. For the second type of structural model, referred to as a flexible model, the platform is represented with beam elements and divided into sections. For each section, the length is approximately 1 m to 2 m, and the hydrodynamic loads are distributed along the platform by integrating panel pressure values for each section in frequency domain as described in Section 3.2. In all these models, the tower is modelled with beam elements.

Nonlinear beam elements with axisymmetric cross-sections are used for the elastic tower, and for the elastic platform in the flexible models. To match the experimental setup, for all four models, the rotor-nacelle assembly is modelled as a rigid body, and the mooring lines are represented as bar elements with the same mooring layout as the experiments.

Structural damping is adopted for the elastic structures modelled with beam elements, including the platform in flexible models and the tower in all models. Herein, stiffness-proportional Rayleigh damping is applied. The damping value is tuned based on hammer tests as described in Section 4.

Table 6
Summary of numerical models in SIMA.

	Rig.ME	Flex.ME	Rig.PFT	Flex.PFT
Platform	Rigid	Flexible (Beam elements)	Rigid	Flexible (Beam elements)
Tower	Beam elements	Beam elements	Beam elements	Beam elements
Wave load model	Morison's equation (ME)	Morison's equation	Potential flow theory (PFT)	Potential flow theory

3.2. Hydrodynamic modelling

The integrated numerical tools typically use potential flow theory or Morison's equation to determine the hydrodynamic loads for FWTs. In this work, as shown in Table 6, both Morison's equation and potential flow theory are applied to different numerical models.

Morison's equation (ME) is often used to calculate wave loads on slender structures, where the diameter D is small compared to the wavelength λ (roughly, $\lambda > 5D$) (Faltinsen, 1993). This work uses Morison's equation to calculate the hydrodynamic loads on the spar platform, and studies the effect of different wave load models on the dynamic response of spar FWTs. Eq. (1) represents the transverse force (f) on a moving cylinder of unit length according to Morison's equation. Herein, the first term is the Froude–Krylov force, the second term gives the added mass contribution ($\dot{v}$) and diffraction effects ($\dot{u}$), and the last term predicts the viscous drag forces.

$$f = \rho\pi\frac{D^2}{4}\dot{u} + \rho C_a\pi\frac{D^2}{4}(\dot{u}-\dot{v}) + \frac{1}{2}\rho C_D D(u-v)|u-v| \tag{1}$$

In Eq. (1), ρ is the fluid density, C_a is the added mass coefficient, u is the transverse wave particle velocity, v is the local transverse body velocity, and C_D is the drag coefficient. The added mass and drag coefficients are usually empirically determined. In this work, a constant added mass coefficient of 1.0 is adopted for the inertial term. As near-field diffraction is neglected, this approach will overestimate loads for shorter wavelengths. This overestimation is especially important close to the natural frequency for the first bending mode.

For the Morison models, the heave hydrodynamic forces are estimated by including the Froude–Krylov force and contribution from the added mass, which can be borrowed from the potential flow solution using a panel method (Karimirad and Moan, 2012). For this spar platform, the zero-frequency heave added mass from the panel method is taken as a representative value. Vertical loads due to dynamic pressure on the tapered section are not considered in the Morison models.

When potential flow theory (PFT) is applied, the 1st-order wave loads are first calculated with the boundary element method software WAMIT (Wamit, Inc., 2006), assuming that the platform is a rigid body. For the rigid model, the hydrodynamic radiation loads from WAMIT can be used directly in the time domain using the Cummins equation (Faltinsen, 1993). However, for the flexible model, the hydrodynamic loads should be distributed along the platform. Fig. 3 shows the procedure of integrating panel pressure to get sectional distributed wave loads for this purpose.

First, as mentioned in Section 3.1, the platform is divided into sections. Next, the panel pressures corresponding to the radiation and diffraction problems provided by WAMIT are output. Then, Eqs. (2) and (3) are used to calculate the added mass (A_{ij}), damping (B_{ij}), and excitation force (X_i) coefficients for each panel based on the pressure.

$$A_{ij} - \frac{i}{\omega}B_{ij} = \frac{1}{\omega^2}\iint_{S_B} n_i\frac{p_i}{\zeta_i}\,\mathrm{d}S \tag{2}$$

$$X_i = \iint_{S_B} n_i p_D\,\mathrm{d}S \tag{3}$$

Subscripts i and j represent different degrees of freedom, ω is the circular frequency, n_i is normal vector on each panel, p_j is the radiation pressure corresponding to unit motion ($\zeta_i = 1$) in each degree of freedom, p_D is panel diffraction pressure, and S_B corresponds to the area of each panel. The wave loads at the respective sections, in the frequency domain, are integrated over the sectional wetted body surface. These sectional wave loads are written in the WAMIT output file format and transferred to the coupled model in SIMA, where the correspondence between sectional wave loads and RIFLEX beam elements is established.

For the Flex.PFT model, this work utilizes the RIFLEX functionality called the Potential Flow Library. With the radiation coefficients and excitation transfer functions, RIFLEX calculates the radiation and diffraction loads in the time domain simulations, using retardation functions for evaluating the radiation loads. The reconstructed radiation coefficients in RIFLEX do not perfectly represent the pitch and roll DOFs or couplings between surge-pitch or sway-roll. The reason for this is that the rotational terms of radiation coefficients for local rotations of small sections are not included. Instead, RIFLEX approximates the moments by integrating the sectional forces in surge and sway, respectively, multiplied by the distance from each section to the origin. The reconstructed coefficients are somewhat larger than their rigid-body counterpart, consistent with previous work on spar FWTs (Silva de Souza and Bachynski-Polić, 2022). Fig. 4 shows the reconstructed pitch added mass: the difference between reconstructed and rigid-body is less than 3% for the whole frequency range.

For all numerical models, the same Morison-type viscous drag force is adopted. The drag coefficient depends on the Reynolds number (Re), Keulegan–Carpenter number (KC), and non-dimensional roughness (Det Norske Veritas, 2010) and is generally estimated empirically. At model scale, the spar experiences high oscillatory Reynolds numbers exceeding 10^5 in most moderate and severe wave conditions. Thus, the non-dimensional transverse drag coefficient is taken to be 0.6 (Det Norske Veritas, 2010), which is a typical coefficient used for spar platforms (Jonkman, 2010; Silva de Souza and Bachynski-Polić, 2022). Drag loads in the platform axial (vertical) direction are not included.

4. Calibration and initial validation

After establishing the numerical models, calibration and initial validation for these models were performed. Different tests are considered, including: static equilibrium tests, pullout tests, hammer tests, and decay tests.

4.1. Static equilibrium

First, the equilibrium position is checked for all models. In the experiments, there is some clearance between the light floaters, and between the floaters and backbone. In the numerical models, the effect of this clearance is addressed by adding extra mass to the platform. For the two rigid models, the extra mass is 4607 kg/m and placed at the centre of gravity of the rigid platform; for the two flexible models, the extra mass is 4000 kg/m and distributed along the platform. The equilibrium vertical position of all numerical models is approximately the same as in the experiments: about 0.4 m above SWL. The horizontal equilibrium positions in all models are approximately the same as the measurements (at 0 m). Furthermore, the mooring line pretension in the numerical models for down-wave and up-wave mooring lines is 1.36E+06 N and 1.18E+06 N, respectively, which agrees well with the measured line pretension as given in Table 3.

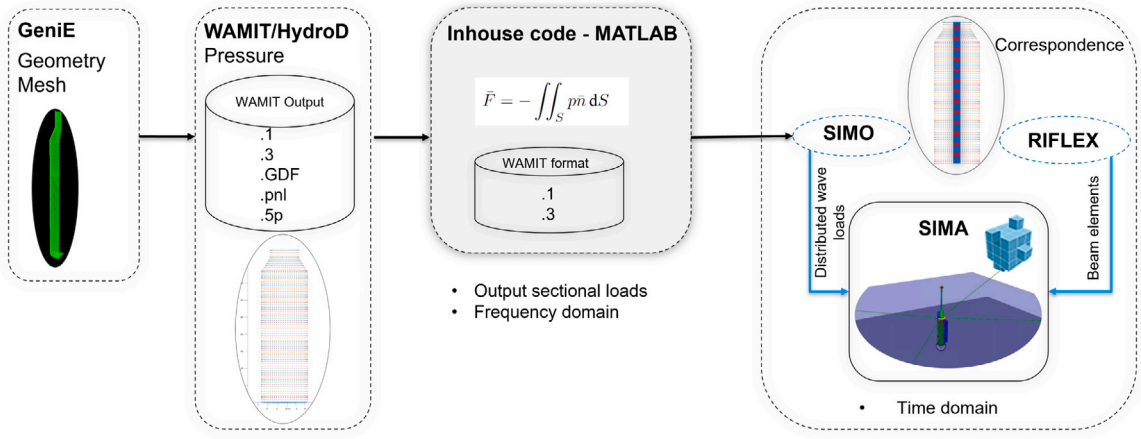

Fig. 3. Schematic of wave loads distribution and Flex.PFT model modelling procedure.

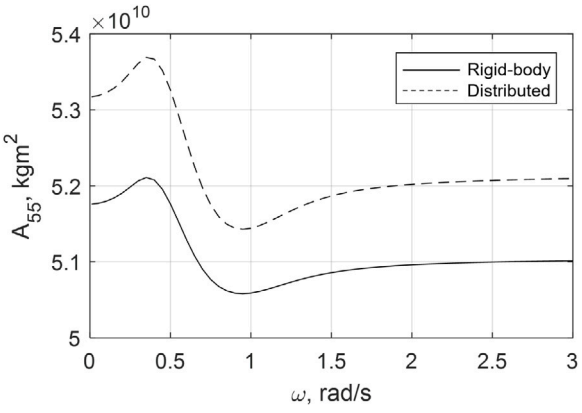

Fig. 4. Comparison of pitch added mass between rigid body and reconstruction.

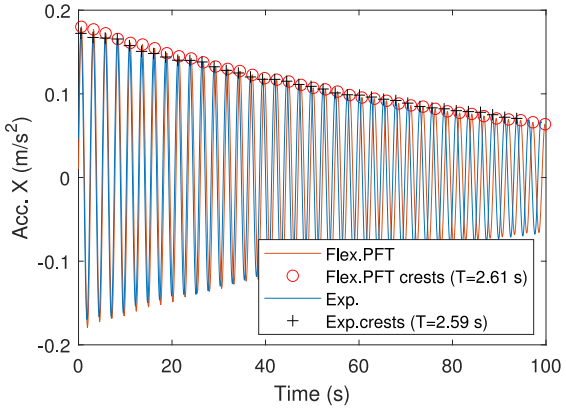

Fig. 5. Decay of the acceleration at the nacelle from a hammer test (Flex.PFT model and experiment).

4.2. Pullout tests

Pullout tests are carried out to further check the numerical modelling of the mooring lines. The same mooring layout used in the experiments is modelled numerically. A series of constant forces are applied on the spar at the same vertical level as the mooring fairlead (4 m above the still water level) to get the displacements in surge and sway, respectively. Then the global linear stiffness is calculated based on mooring line tension and displacement. The calculated stiffness for the whole mooring system in the surge and sway directions is 121.9 kN/m and 97.7 kN/m, respectively. The numerical stiffness for the mooring system agrees well with the measured value from pullout tests as given in Section 2.1.

4.3. Hammer tests

Hammer tests are performed for all numerical models to check the first bending mode frequencies. A force (along the x axis) with 0.1 s time duration is imposed on nacelle to excite the natural modes. Then, the acceleration of the nacelle is analysed to get the first bending mode natural frequency. To match the experimental results, the Young's modulus for the tower in the flexible models is increased by 5%. The stiffness-proportional structural damping coefficient for the tower is tuned to 0.0025 s for all numerical models. For the two flexible models, stiffness-proportional structural damping with coefficient 0.001 s is applied to the flexible cylindrical platform.

Table 7
First bending mode natural period obtained from decaying acceleration from hammer tests.

	Natural period (s)	Discrepancy (%)
Exp.	2.59	–
Rig.ME	2.57	−0.77
Flex.ME	2.66	2.70
Rig.PFT	2.50	−3.47
Flex.PFT	2.61	0.77

A band-pass filter was applied to the acceleration time series with focus on the response around the first fore-aft bending mode frequency. Fig. 5 shows the decaying acceleration in the x direction measured at nacelle after a hammer test on the nacelle. Table 7 compares the calculated first bending mode frequencies between numerical and experiment results. Herein, as expected, the flexible models have larger natural periods in bending than the rigid models, despite the increased Young's modulus for the tower in the flexible models. The numerical models all have natural periods within 4% of the experimental results.

4.4. Decay tests

Decay tests are performed for all numerical models to check the natural periods of the rigid degrees of freedom (DOF) of interest (surge, heave, and pitch). In the simulations, an initial offset is imposed for each degree of freedom, then the platform is released and gradually returns to its equilibrium position in the absence of waves and wind.

Table 8
Comparison of motion natural periods between numerical results and experimental results.

	Surge (s)	Discrepancy (%)	Heave (s)	Discrepancy (%)	Pitch (s)	Discrepancy (%)
Exp.	128.00	–	30.70	–	33.70	–
Rig.ME	131.19	2.5	30.61	−0.3	33.03	−2.0
Flex.ME	129.78	1.4	30.70	0.0	34.05	1.0
Rig.PFT	128.77	0.6	30.61	−0.3	32.53	−3.5
Flex.PFT	128.73	0.6	30.67	−0.1	34.09	1.2

To calibrate the numerical models, the damping has been tuned to match the experimental damping ratios by adding a global linear damping matrix. First, a linear damping of 7.0E+07 Ns/m for heave is adopted for all numerical models. For the potential flow models, this linear damping is in addition to the radiation damping from the potential flow solution. Linear damping in yaw of 1.3E+07 Nsm is also added to all numerical models to avoid unrealistic resonant responses. For the Flex.PFT model, a extra linear pitch damping of 2.0E+08 Nsm is implemented to compensate for the discrepancy in the radiation loads in RIFLEX. This discrepancy arises from both the evaluation of the radiation loads using retardation functions (of limited duration) in the time domain, and from neglecting the rotational terms of radiation coefficients for local rotations of small sections. In terms of viscous forces, the same quadratic heave damping of 1.0E+5 Ns^2/m^2 is added to all models.

Fig. 6 shows the decay time series for surge, heave, and pitch motion. The natural periods for each DOF are obtained from the motion time series based on fast Fourier transform (FFT) analyses and compared in Table 8. Overall, the natural periods for surge, heave and pitch predicted by both the flexible models and rigid models all match the experiment results well, with discrepancy below 4%. For the surge decay, clear coupling between surge and pitch motions can be seen in the experiment and all numerical models. The Morison models, especially Rig.ME, overestimate the surge natural period. The reason for this discrepancy is likely due to the choice of added mass coefficient. Compared to the experiment, all models overestimate the linear damping in the surge degree of freedom (the overestimation is less than approximately 30%), except for the Flex.PFT model, which captures linear surge damping close to the measured results. For the heave decay, all numerical models capture the period and motion amplitude fairly well, and the tuned damping coefficients match the still-water experiments well.

In the case of pitch, coupling with the surge motion is again seen. The pitch natural period is slightly overestimated by the flexible models and underestimated by the rigid models. The linear pitch damping in all models and in the experiment is small: the damping ratios range from 0.61% to 0.95%. The Rig.ME model shows linear pitch damping very close to the experimental result, while other three models tend to overestimate the linear pitch damping (by less than approximately 55%). Overall, for this 10 MW spar-type floating wind turbine, the effect of platform flexibility on the natural periods of rigid body motions is small, unlike the behaviour observed for the heave natural period of a TLP floating wind turbine (Silva de Souza and Bachynski, 2020).

In order to evaluate the structural responses in the flexible models, the time series of strains obtained from the pitch decay tests are plotted in Fig. 7. For strain 2 and strain 3, the numerical models predict the strain response quite well. It should be mentioned that it is difficult to obtain identical initial conditions in SIMA as in the experiments, which causes differences between numerical and experimental results. Consistent with the pitch motion, the numerical models show larger damping at the pitch natural frequency. The numerical models tend to overpredict the strain amplitudes for strain 1, and this is seen to a greater extent for tests in waves. The reason for this discrepancy is not clear, and could be related to differences in the mass distribution or stiffness model. In the subsequent results, only strain 2 is shown for brevity.

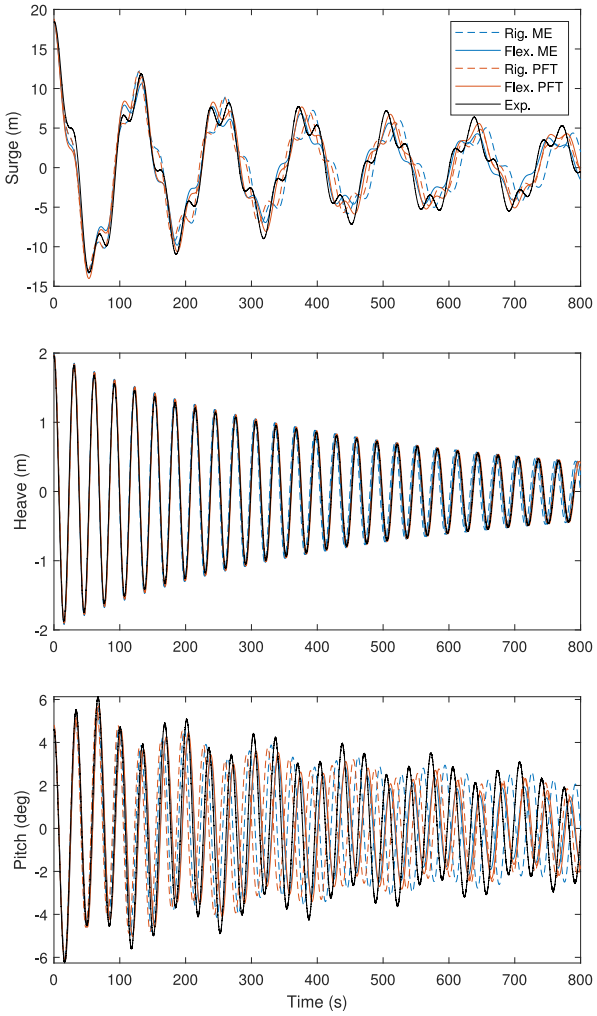

Fig. 6. Comparison of motion decay time series between numerical simulations and model tests.

5. Results and discussion

In this section, a detailed numerical analysis of the responses to a series of regular wave cases as well as irregular sea states is carried out.

5.1. Response in regular waves

Time-domain simulations are performed considering regular waves propagating along the x-axis. The wave amplitudes and periods were measured from the wave calibration campaign, as shown in Table 4. Based on these measured values, sinusoidal monochromatic waves are obtained using linear wave theory and used as input for the simulations in all numerical models. A limited time window is considered for the analysis of the response. For experiments, the time windows before the wave reflections arrive from the beach are used; for simulations, the time windows after start-up transient behaviour are considered.

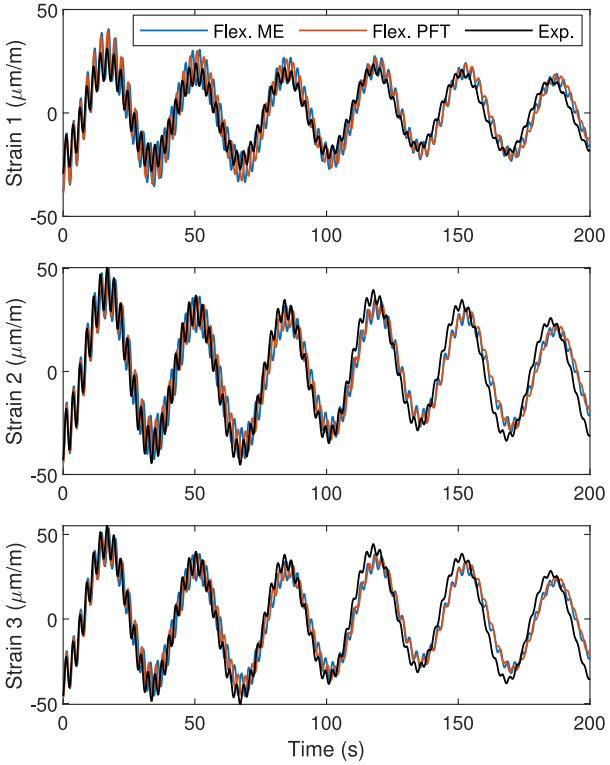

Fig. 7. Comparison of strain between numerical simulations and model tests during the pitch decay tests.

5.1.1. First order response

Fig. 8 shows an example of a time series comparison for pitch, strain 2 and tower base bending moment between numerical results and experimental results. The wave period is 10.33 s and the wave steepness is 2%. The response for this regular wave condition is almost linear with negligible higher order components (Leroy et al., 2022a). The wave-frequency pitch motion from the numerical models agrees with the experiment results, while the Rig.ME model shows large response around the surge and pitch natural periods. Similarly, for strain 2 and the tower base bending moment, all numerical results are very close to the experiment results.

In order to investigate the first order responses in all regular waves, the response amplitude operators (RAOs) are obtained based on Fourier analysis for the responses. The RAOs are equal to the harmonic of the response at the corresponding wave frequency divided by the first order wave amplitude. Herein, motions (surge, heave, and pitch), strains and tower base bending moments are considered.

The RAOs under regular waves with steepness 2% are presented here. Fig. 9 shows the motion RAOs of surge, heave and pitch for different wave conditions. For surge and heave motion, all four numerical models agree well with the experiments. For the pitch motion, the flexible models and experiments agree well across all wave periods. The rigid models tend to overpredict the pitch response for large wave periods, and the underlying cause for this difference remains unclear.

Fig. 10 shows the RAOs for strain 2 and the tower base bending moment under regular wave conditions with steepness 2%. For strain 2, the Flex.PFT model underestimates the response, but shows the correct trend compared to the experimental results. When wave periods are longer than about 8 s, the Flex.ME model predict similar responses as the Flex.PFT model. For low wave periods, the Flex.ME model overestimates the response due to the limitations of the slender body assumption.

For tower base bending moment M_y, similarly to strain 2, both potential flow models capture the trends from the experiments well. For

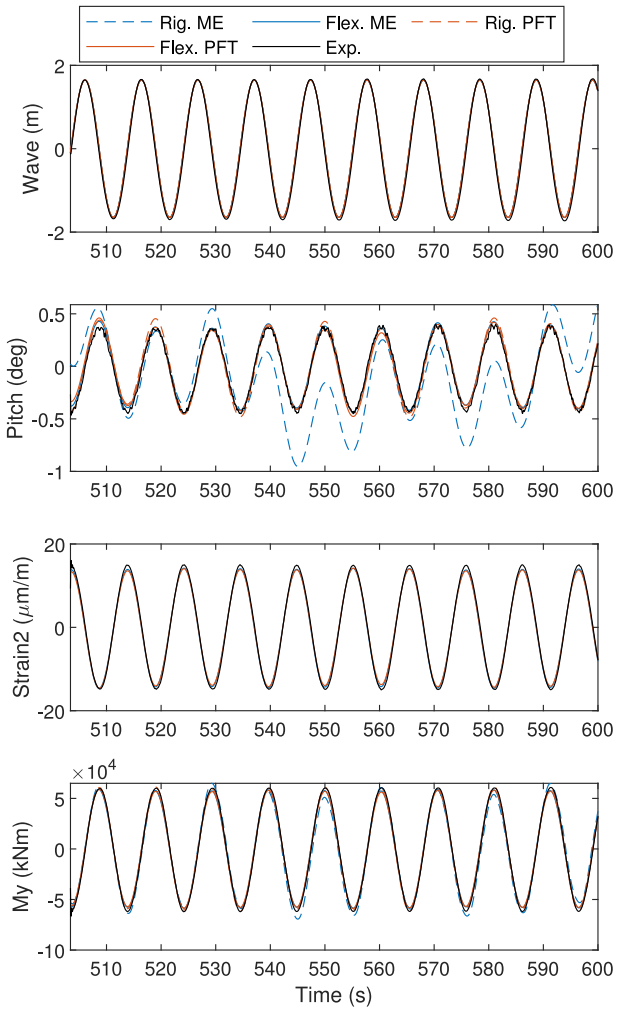

Fig. 8. Responses for regular wave EC8 with wave steepness 2%, Numerical models compared to experiments.

short wave periods, both ME models overestimate the linear response, again, due to the limitations of the slender body assumption. For long wave periods, both flexible models predict lower linear response, while the two rigid models have good agreement. The responses in long waves are consistent when the structural models are the same.

Overall, the strain 2 and tower base bending moment responses are consistently under-predicted by the flexible numerical models. When the wave period is longer than approximately 8 s, where the slender body assumption is satisfied for Morison's equation, the difference in strain 2 between flexible models and experiments is within 10%.

5.1.2. Nonlinear response

After studying the first order response, this section further discusses the nonlinear responses in the numerical results, particularly strain 2 and the tower base fore-aft bending moment.

Fig. 11 shows the response of strain 2 and tower base bending moment under two different wave conditions, where the 2nd-order and 3rd-order nonlinear responses are observed from the experiment, respectively (Leroy et al., 2022a). The results show that the numerical models are not able to capture the nonlinear response. One of the reasons is that the wave input used for numerical simulations is based on linear wave theory, while the experimentally measured wave for these two conditions is strongly nonlinear. For the models based on potential flow theory, higher order wave loads are not included in the modelling, except for the contributions from viscous drag loads. For

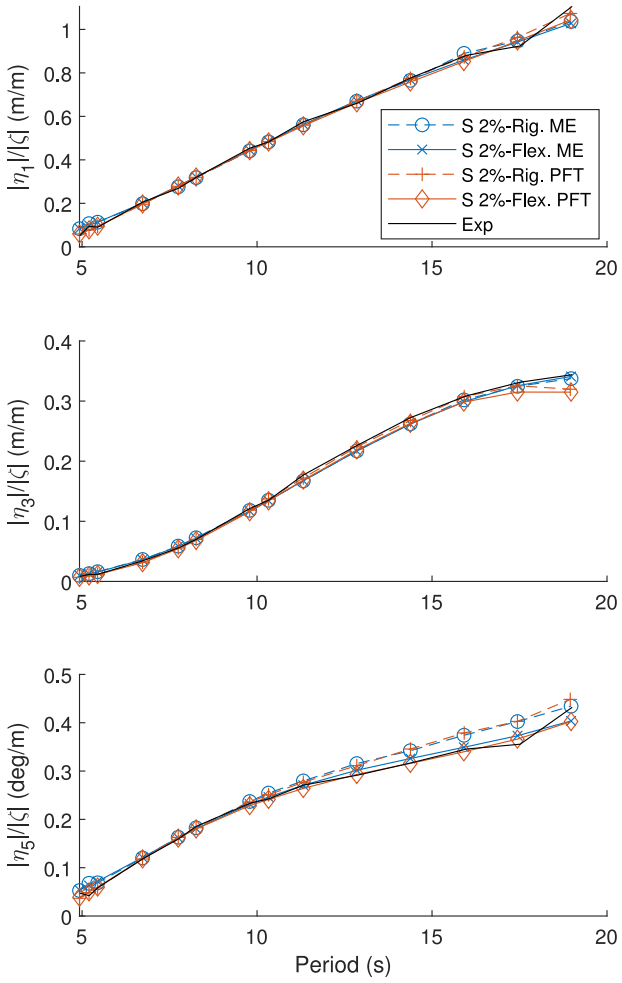

Fig. 9. Motion RAOs under wave series 2%.

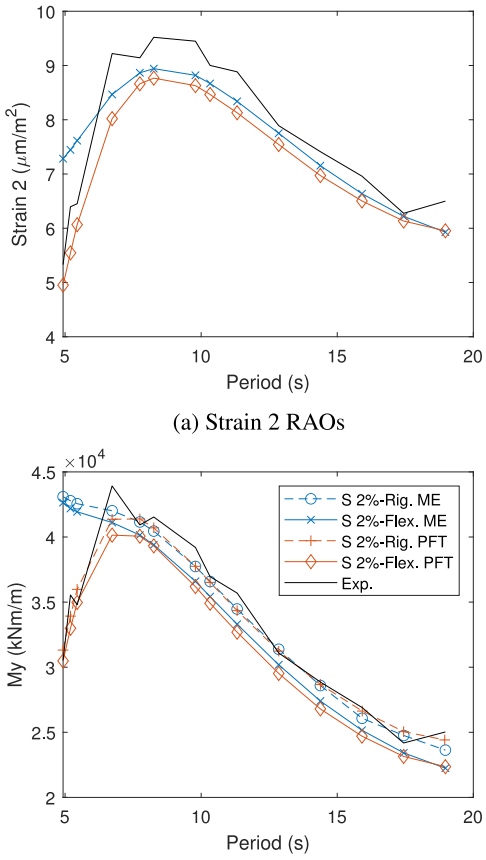

Fig. 10. RAOs for strain 2 and tower base fore-aft bending moment My under wave series 2%.

the Morison models, the wave loads are integrated up to the first order free surface, which introduces some second order loads in addition to nonlinear contributions from viscous drag. In addition, the 1st bending mode frequency slightly differs in different models and experiments, meaning that the structural resonant response in the numerical models at the applied wave frequency is not fully excited.

5.2. Response in irregular waves

In order to further assess the performance of the numerical models in irregular waves against experimental results, time-domain simulations are performed with the irregular wave conditions shown in Table 5. The measured experimental wave time series obtained from the wave calibration campaign, after removing high frequency (higher than 10 times the wave peak frequency) components, were used as the input for numerical simulations. The wave kinematics in SIMA are reconstructed based on the superposition principle, treating all components as linear. Furthermore, the kinematics from mean water level to wave surface, which are used for the Morison drag term in PFT models and the integration of wave forces in ME models, are considered by keeping the potential constant. All SIMA simulations are carried out for the same time duration as the experiment.

The numerical response time series of are first compared to experimental results. Fig. 12 shows the wave elevation, pitch motion, strain 2, and tower base loads under wave condition SS8 (the 50-year return period sea state). The pitch time series shows that the responses at the wave frequency agree well with the experimental results. For the low-frequency response, a difference in the phase leads to less consistency between numerical models and experiments for a small wave group.

The comparison of strain 2 shows that the Flex.PFT numerical model can capture the strain response quite well for both large and small wave groups. However, the flexible model with Morison's equation shows a large persistent discrepancy compared to experiment, because of the overprediction of the response at 1st bending mode frequency. This discrepancy is particularly significant after a large wave group impact around 2020 s. For the tower base fore-aft bending moment, similarly to strain 2, the distributed potential flow model can predict the response well, while the Flex.ME model differs compared to experimental time series. This overestimation is also seen in the other two models after a large wave group, meaning that large response at 1st bending mode frequency is excited due to the partial nonlinear effects that are included in the numerical models.

Next, a more detailed analysis of the responses to irregular waves is carried out. The following response metrics are chosen to investigate different response components. First, the power spectral density (PSD) is used to investigate the responses in different frequencies. In order to quantify the responses in different frequency ranges, the power spectral density sum (PSD sum) which keeps some frequency information is adopted as a new response metric. The PSD sum is defined as the integration of the one-sided, unsmoothed, discrete power density functions of the response in the frequency range of interest (Robertson et al., 2020). The frequency limits are determined based on the ranges over which the wave spectra are defined and consideration of the response frequencies of interest. Later, the responses near the 1st bending mode

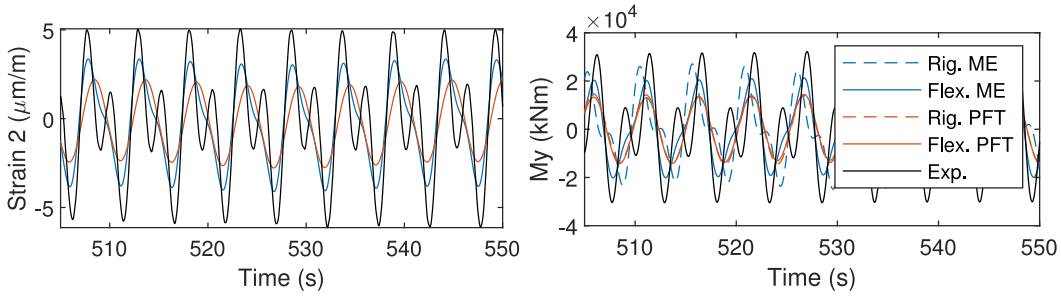

(a) Wave period 5.2 s, 2% wave steepness (2 times the 1st fore-aft bending mode period)

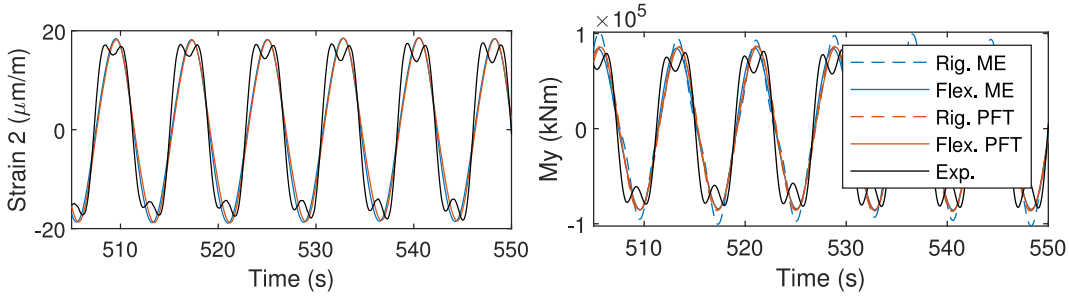

(b) Wave period 7.75 s, 4% wave steepness (3 times the 1st fore-aft bending mode period)

Fig. 11. Response of strain 2 and tower base bending moment under regular waves.

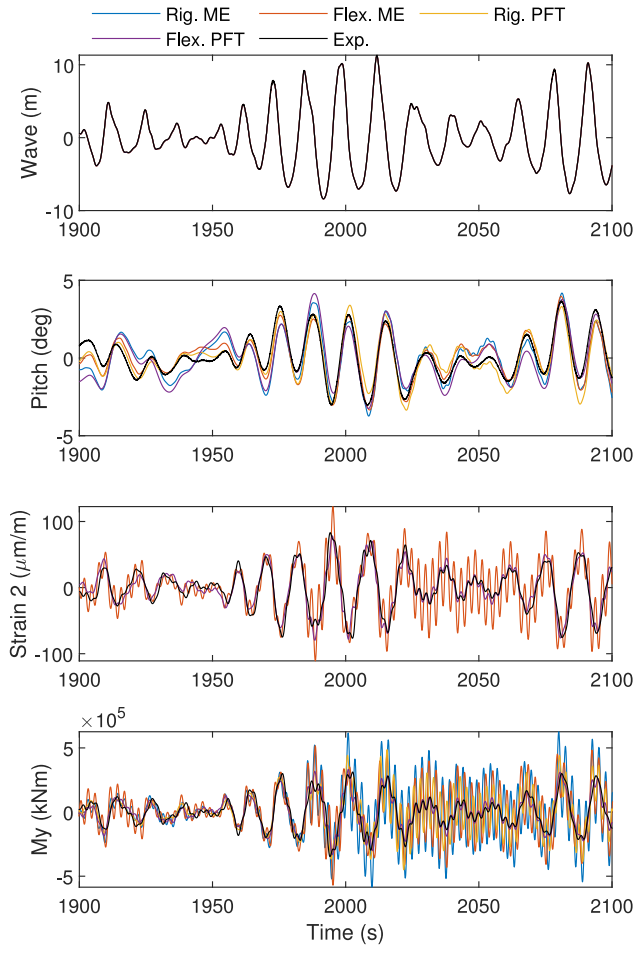

Fig. 12. Responses (wave elevation, pitch, strain 2 and tower base fore-aft bending moment) in sea state SS8 (50-year return period), numerical results compared to experimental results.

natural frequency are also compared to the experimental results to check the springing and ringing events.

Three sea states SS2 (T_p = 6.0 s, H_s = 1.5 m), SS5 (T_p = 10.0 s, H_s = 4.0 m), and SS8 (T_p = 13.8 s, H_s = 10.9 m) are selected and presented in the following analysis.

5.2.1. Power spectral density

The spectra were calculated based on the same time window, around 1.8 h, for all numerical and experimental results. The transient stage at the wave-maker start is not included in the analysis. To ensure all time series of experiments and simulations have identical discretization in time, all time series are first cut and sampled with a time step of 0.01 s. The pitch motion, strain 2 and tower base bending moment are considered.

Fig. 13 compares the PSDs of wave and pitch motion between numerical models and experiments. The reproduced waves in SIMA generally agree quite well with the experimentally measured calibrated waves. For the pitch motion, the wave-frequency response excited by linear wave excitation is reproduced quite well by all numerical models. In the low-frequency range, a large contribution is found, particularly at the pitch natural frequency in both numerical models and experiments. The pitch and surge natural frequencies are outside the wave frequency range and can be excited by nonlinear wave loads. The PFT models are based on linear potential flow theory (the quadratic transfer function, QTF, is not included), and the nonlinear wave loads are from the viscous drag loads. For the Morison models, the nonlinear wave load contributions are from integrating the loads up to the first-order free surface and from viscous drag. Overall, these four numerical models do not capture the complete second-order or higher-order wave loads. In addition, damping plays a large role in the resonant response. Due to the balance of excitation and damping, which vary with the sea state due to the relative velocity term in the Morison drag force, the comparison of low-frequency pitch responses between numerical models and experiments does not show a consistent trend for all sea states. To improve the estimation in the low-frequency range, additional effort is needed to apply nonlinear wave loads and to better quantify the damping.

Fig. 14 compares the PSDs of strain 2 and tower base fore-aft bending moment between numerical models and experiments. First,

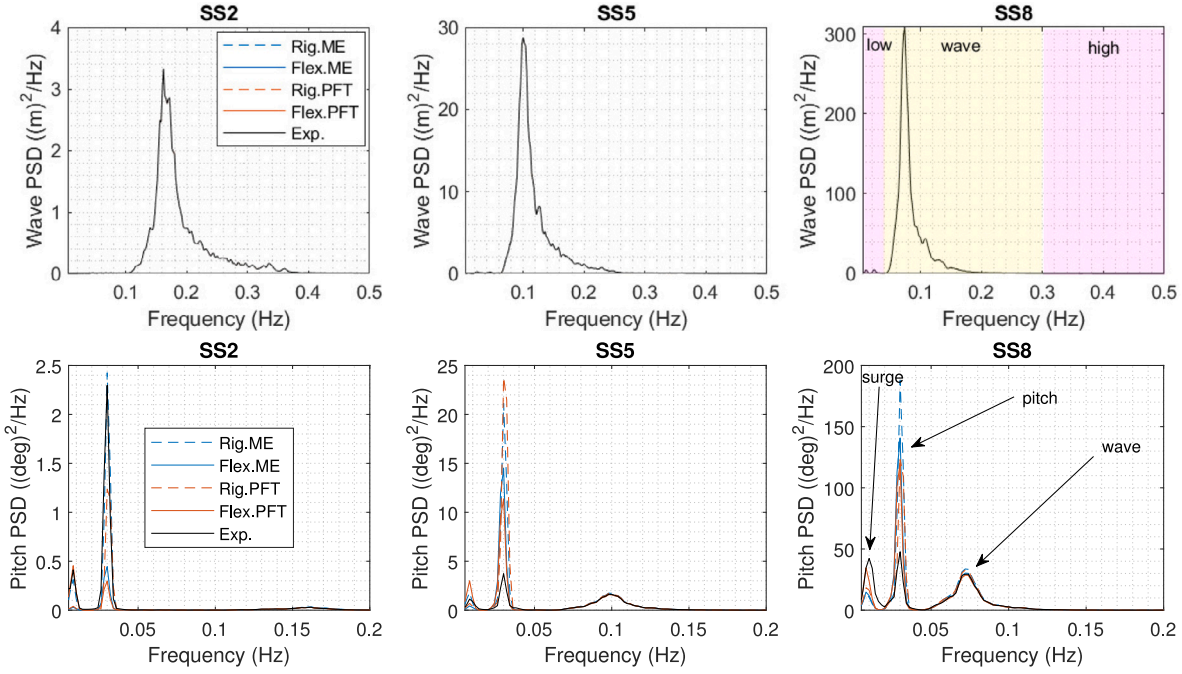

Fig. 13. Power spectral density of wave and pitch motion in irregular waves (SS2,SS5, and SS8), numerical models compared to experiments.

for all numerical and experimental results, significant responses are observed around the first order bending mode natural frequency, which is higher than around 0.3 Hz and outside the wave frequency range, as illustrated using the green coloured regions in the plot. The four numerical models differ regarding the 1st bending mode frequency, which is one of the reasons that the predictions for the responses around the resonant frequencies are less consistent.

For strain 2, the Flex.PFT model can predict the response at the 1st bending mode frequency well, especially under irregular waves SS8. However, the Flex.ME model shows large overprediction for the 1st bending response over all sea states because these frequencies fall outside the slender body assumption. Thus, suitable wave load modelling is important for studying the 1st bending mode response. The distributed potential flow model works well here.

For the tower base bending moment, as for strain 2, the Flex.PFT model works quite well in the 1st bending mode frequency range. Results show that for SS8, the response amplitude at the peak frequency is very close to experimental results. Generally, the Rig.PFT model also predicts the tower base bending moment amplitude well, despite the slight offset in the spectra compared to experiments. Overall, there is a consistent under-estimation in both PFT models in all sea states. For the severe wave condition SS8, compared to experimental results, the discrepancy for the response at the peak frequency within the 1st bending mode frequency range in Rig.PFT and Flex.PFT model is about −5.48% and −21.75%, respectively. Similarly to the strain 2, the two ME models heavily overestimate the tower base bending moment at the first bending natural frequency.

At the wave frequency, all numerical models are able to predict the structural responses (strain 2 and tower base bending moment) quite well compared to experiments. In the low-frequency range, the structural responses are mainly dominated by the low-frequency contributions related to pitch motions at the pitch natural frequency. Thus, both strain 2 and the tower base bending moment have similar results as the low-frequency pitch motion when compared with experimental results: large overprediction at the pitch natural frequency is seen. The reason for this is the same as explained for the low-frequency pitch motion.

5.2.2. PSD sum for response

In order to further investigate the response in different frequency ranges, the PSD sum was calculated based on the power spectral density and presented in this section. Herein, the structural response strain 2 and tower base bending moment are considered.

The integration limits for PSD sums are illustrated using the coloured regions in the plots in Fig. 14. In this work, the different frequency ranges for all sea states are:

- The 1st bending mode frequency range: green region, 0.3–0.5 Hz.
- Wave-frequency range: yellow region, 0.04–0.3 Hz;
- Low-frequency range: pink region, 0.005–0.04 Hz;

The PSD sums for the PFT models in the 1st bending mode frequency range are compared with the experiments and plotted in Fig. 15. In this frequency range, compared to experiments, ME models have very large overprediction for both strain 2 and tower base bending moment and are therefore not presented. As shown in the power spectral density, the PFT models consistently underestimate the response in all sea states. This could be caused by incomplete higher order wave loads estimation.

Fig. 16 compares the PSD sums in the wave-frequency range for strain 2 and tower base loads between different models and experiments. For sea state SS2, the ME models predict larger responses than experiments. This is caused by the load overestimation using Morison's equation in the frequency range between 0.2 Hz and 0.3 Hz, where larger response is predicted as shown in Fig. 14. For the wave conditions SS5 and SS8, all models except the Flex.PFT model show wave-frequency responses that are similar to the experiments, while there is a consistent underprediction in the Flex.PFT model. For the 50-year return period sea state, the difference is approximately −10%. This underestimation for strain 2 and tower base loads is also found in the RAOs obtained from regular waves. However, Fig. 17 shows the PSD sums for motion (surge, heave and pitch) in sea state SS8. The Flex.PFT model can capture the surge, heave and pitch response quite well. The other three models overestimate the wave-frequency pitch motion, which could increase the structural responses.

Fig. 18 compares the PSD sums in the low-frequency range for the strain 2 and tower base fore-aft bending moment between numerical models and experiments. The low-frequency PSD sums are much lower

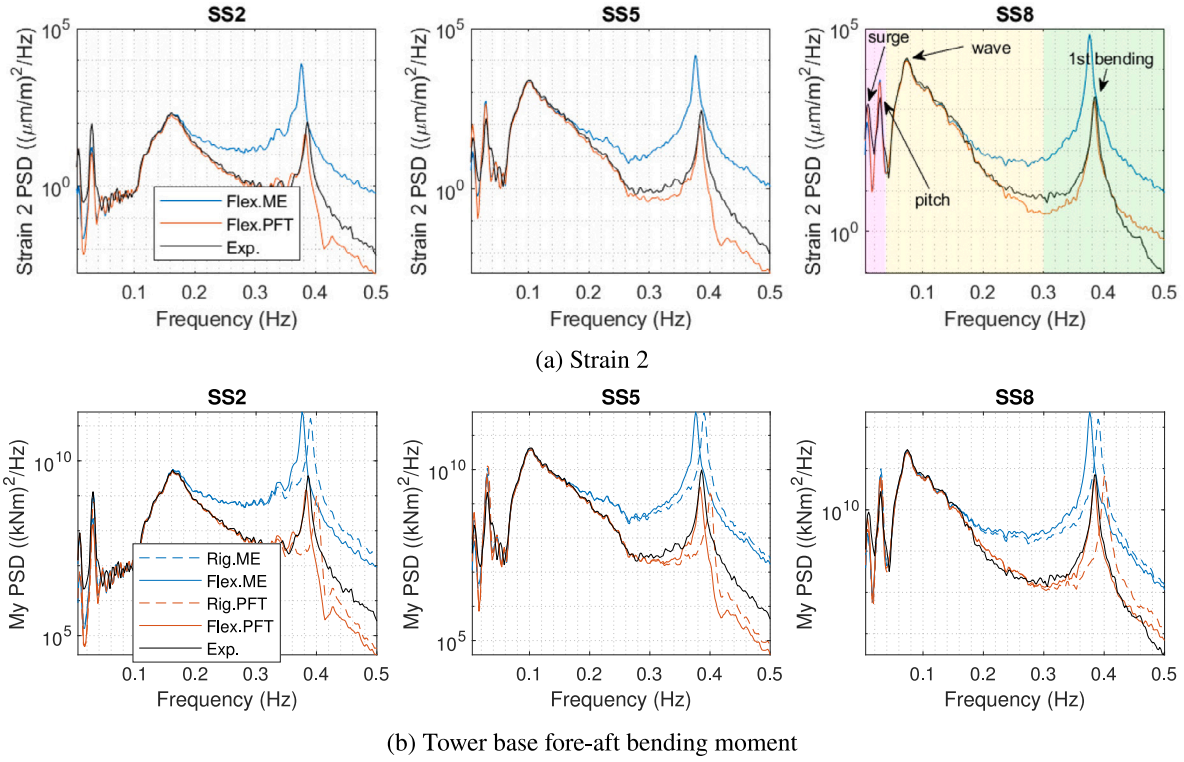

Fig. 14. Power spectral density (log scale ordinate) for strain 2 and tower base fore-aft bending moment in irregular waves (SS2, SS5, and SS8), numerical models compared to experiments.

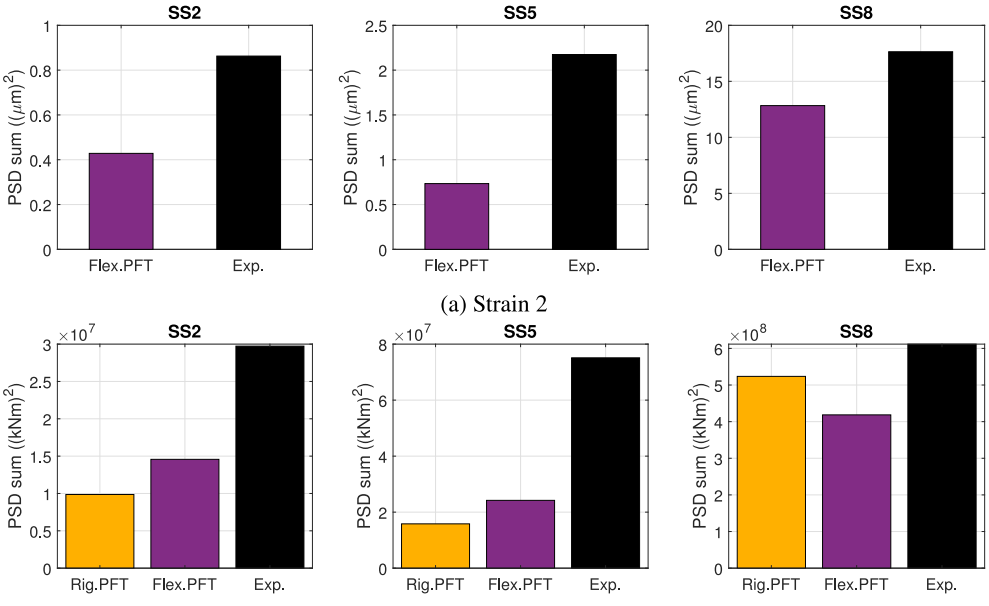

Fig. 15. PSD sum in the 1st bending mode frequency range for strain 2 and tower base fore-aft bending moment in irregular waves (SS2, SS5, and SS8), numerical models compared to experiments.

than the wave-frequency PSD sums. For sea state SS2, due to the underprediction of the low-frequency pitch motion, all models show smaller structural response than the experiment. For the other two sea states, the overprediction of low-frequency pitch motion (particularly around the pitch natural frequency) by all models, makes the strain 2 and tower base bending moment overestimated. As previously discussed, none of these models captures the complete second-order or higher-order wave loads for the low-frequency region. Besides, due to resonance, deviations in damping can result in differences between simulations and experiments as well.

5.2.3. Response around first bending mode frequency

The resonant response at the 1st bending mode frequency could be triggered by high-frequency and higher-order nonlinear hydrodynamic loads. Springing/ringing events were observed in the experiments (Leroy et al., 2022a). In order to evaluate the performance of

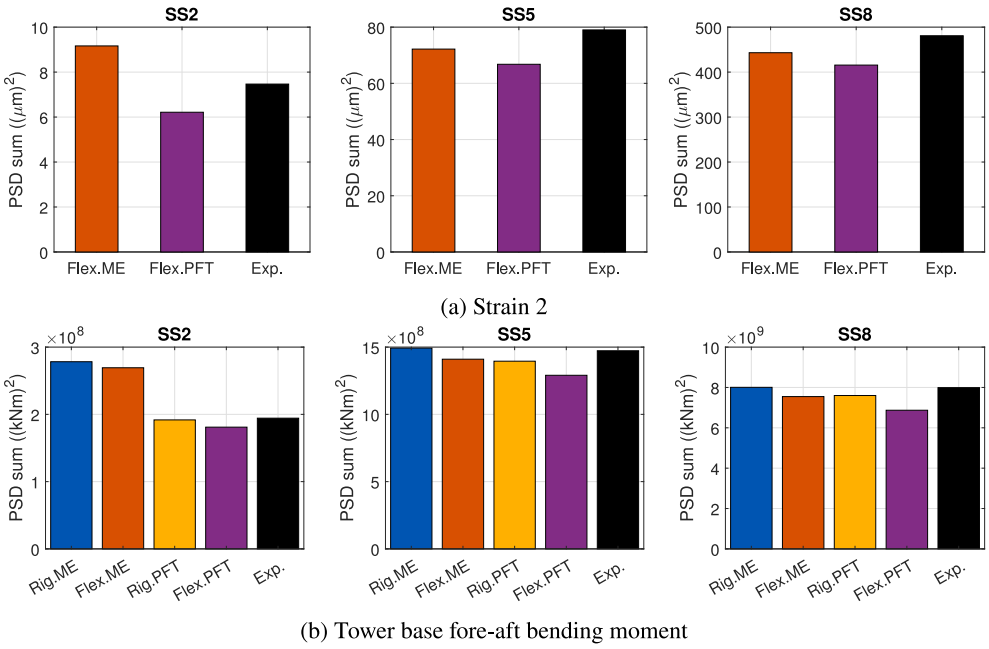

Fig. 16. PSD sum in wave-frequency range for strain 2 and tower base fore-aft bending moment in irregular waves (SS2, SS5, and SS8), numerical models compared to experiments.

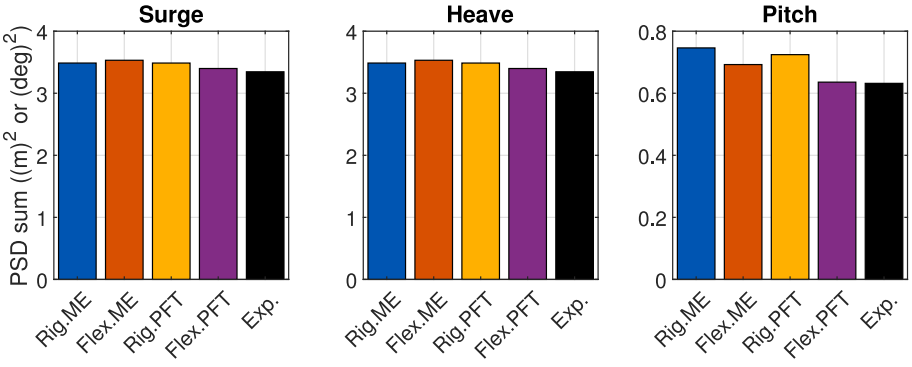

Fig. 17. PSD sum in wave-frequency range for motion in irregular wave SS8, numerical models compared to experiments.

numerical models, the numerical results were first band-pass filtered around the 1st bending mode natural frequency corresponding to each model. In this section, the strain 2 and tower base bending moment responses are used to study the springing/ringing events.

Resonant responses have been observed in simulations and experiments under the irregular waves. Fig. 19 compares the response of strain 2 and tower base bending moment at the 1st fore-aft bending natural frequency. The wave condition is the 50-year return period sea state SS8. The wave time series is plotted together with the response to identify the wave groups. The experiments show a series of resonance events, and each event can be associated with a large wave group. In all numerical models, resonance is also excited in some time windows. The ME models tend to heavily overpredict the 1st bending mode structural responses. For models based on potential flow theory, due to the lack of the second-order wave loads, the 1st bending mode response is not well excited most of the time. Compared to the other three models, the Flex.PFT model shows comparable responses with the experimental results for strain 2 and tower base bending moment, which are visible around 4400 s, 5400 s, and 5850 s.

Next, a shorter time window is selected to present the results. The responses in an intermediate sea-state SS5 (T_p = 10.0 s, H_s = 4 m) and the most severe sea-state SS8 (50-year return period, T_p = 13.8 s, H_s = 10.9 m) are plotted in Fig. 20.

In sea state SS5, a growing bending mode response in tower base bending moment and strain 2 starting from 4360 s is observed in the experiment results. In the numerical models, both strain 2 and the tower base loads are progressively increasing. Again, presumably due to lack of the nonlinear wave loads, the PFT models underestimate this response as found in the PSD in Fig. 14 as well.

For sea state SS8, the response in the time window from 5800 s to 6000 s is presented in Fig. 20. The strain 2 and tower base bending moment responses are much larger compared to the sea state SS5. Triggered by the large wave group starting from 5800 s, all models and experiments captured the resonance responses which decreased gradually. Herein, all numerical models overestimate the response. In the PFT models, the reason could be the insufficient viscous damping; for the ME models, the main reason is that the slender body assumption is no longer valid in this range of frequencies. Compared to the other three models, the Flex.PFT model tends to predict a comparable 1st bending mode response of strain 2 and tower base bending moment.

Overall, in both cases, the resonant (springing/ringing) oscillations are clearly visible in both strain 2 and tower base bending moment responses. Persistent large overestimation is seen in the ME models in all sea states, which is also shown in PSD in Fig. 14. The Flex.PFT model predicts comparable responses with the experimental results.

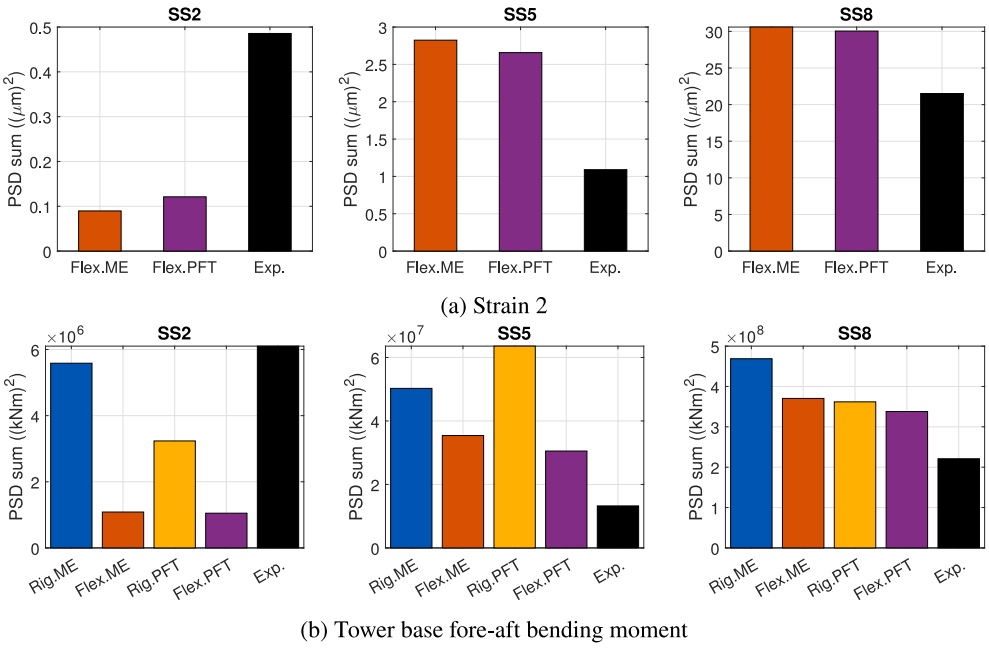

Fig. 18. PSD sum in low-frequency range for strain 2 and tower base fore-aft bending moment in irregular waves (SS2, SS5, and SS8), numerical models compared to experiments.

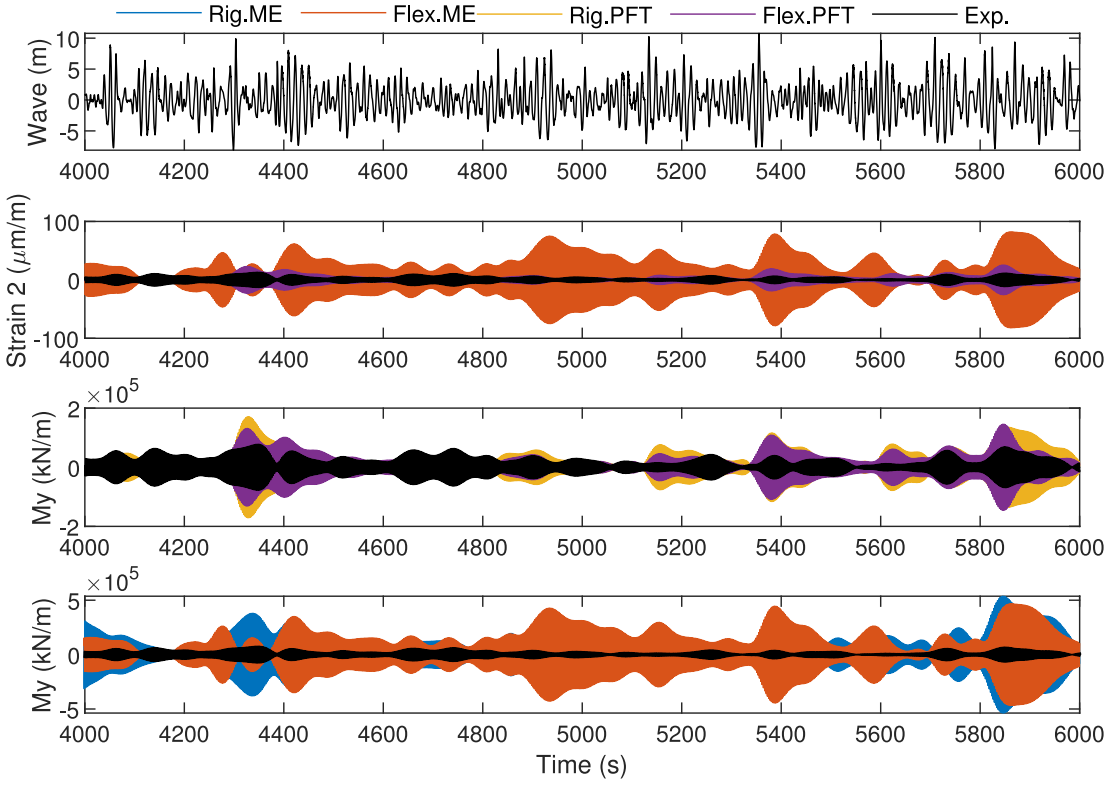

Fig. 19. First order bending responses for strain 2 and tower base bending moment in SS8 (T_p = 13.8 s, H_s = 10.9 m), numerical models compared to experiments.

6. Conclusion

This work presents numerical investigations and comparison against experiments for a 10 MW Froude-scaled experimental spar FWT. In this paper, four coupled numerical models have been used, which are: rigid platform with Morison's equation, flexible platform with Morison's equation, rigid platform with potential flow theory, flexible platform with potential flow theory. Numerical reproductions of wave tank tests including hammer tests, decay tests, regular wave tests, and irregular wave tests are considered for calibrating and validating the numerical models.

First, the first bending mode natural frequency in numerical models was checked by hammer tests to match the experimental results. In the free decay tests, all numerical models were found to predict the natural periods for rigid body motions very well compared to the experiments (within 4% discrepancy). The damping was tuned to match the experimental damping ratios. The flexible models have larger pitch

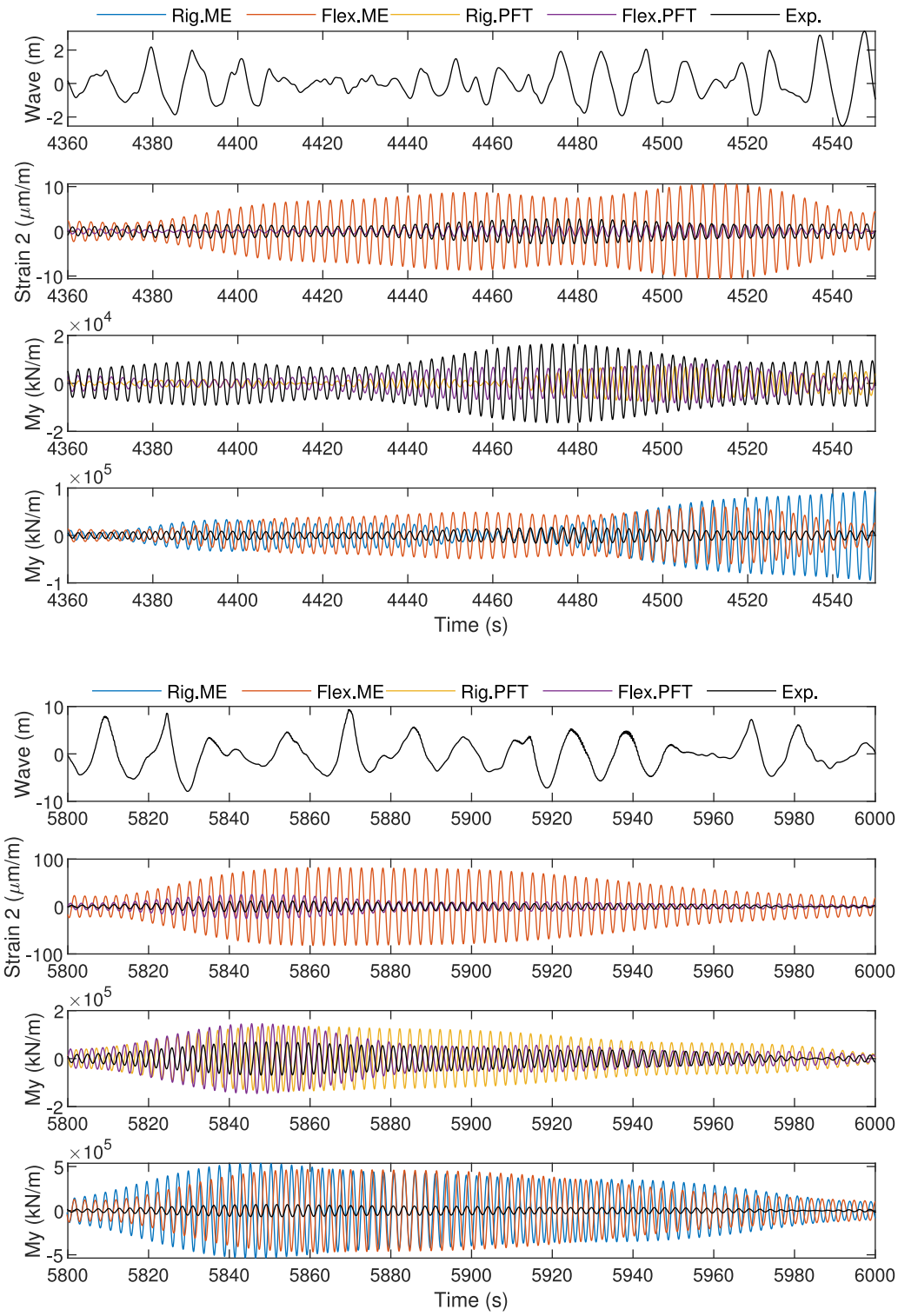

Fig. 20. First order bending responses for strain 2 and tower base bending moment, numerical models compared to experiments. Top: SS5 (T_p = 10.0 s, H_s = 4.0 m), bottom: SS8 (T_p = 13.8 s, H_s = 10.9 m).

natural periods than rigid models, but this change due to considering platform flexibility is less than 4% for this spar FWT.

The wave-frequency surge and heave motion RAOs are all well predicted by all numerical models. For the pitch motion RAOs, the rigid models slightly overpredict for long wave periods, while the two flexible models show good agreement with the experiments. For the strain on the platform and the tower base loads, the Morison models all overpredict the linear response for short wave periods due to the limitations of the slender body assumption. When the wave period is longer than approximately 8 s, the two flexible models slightly underestimate the linear structural response. However, the response in long waves is consistent when the structural models are the same, and shows very good agreement with experiments regarding the trend.

In irregular waves, similarly to the linear response in regular waves, the wave-frequency motion, strain, and tower base bending moment

response agree fairly well with the experimental results. The low-frequency responses around the surge and pitch natural frequency are observed in all numerical models and in the experiments. Overall, all numerical models underpredict the total low-frequency response (pitch motion, strain, and tower base bending moment) for the weak wave condition, but overestimate these responses in the mild sea state and worst sea state (50-year return period sea state). This was traced to the estimation of nonlinear hydrodynamic loads. The models based on linear potential flow theory only include nonlinear wave loads due to viscous drag loads. The Morison models consider nonlinear contributions from viscous drag and integrating wave loads up to the first-order free surface. In addition, the reconstructed irregular wave is based on a linear superposition principle, thus these models are not able to capture complete nonlinear wave loads.

For the strain on the platform and the tower base bending moment, a large contribution from response around the 1st bending mode frequency is seen in all numerical models and experiments in irregular waves. Both Morison models highly overestimate the 1st bending mode response under the restrictions imposed by the slender body assumption. The distributed potential flow model shows reasonable agreement with the experiments.

In conclusion, all models can capture the system natural frequencies and the wave-frequency linear responses (motion, tower base fore-aft bending moment, and strain on the platform in flexible models) well compared to the experiments, except for the fact that the Morison models overpredict the regular wave responses for short wave periods. Overall, the distributed potential model shows the best agreement with the measurement for the structural response around the 1st bending mode frequency. It is apparent that inclusion of higher order wave loads and nonlinear wave kinematics is needed to enhance the accuracy of the model.

CRediT authorship contribution statement

Xiaoming Ran: Methodology, Software, Validation, Investigation, Data curation, Formal analysis, Visualization, Writing – original draft. **Vincent Leroy:** Investigation, Resources, Writing – review & editing, Supervision. **Erin E. Bachynski-Polić:** Conceptualization, Methodology, Software, Resources, Writing – review & editing, Supervision, Funding acquisition.

Declaration of competing interest

The authors declare that they have no known competing financial interests or personal relationships that could have appeared to influence the work reported in this paper.

Data availability

Data will be made available on request

Acknowledgements

This work is performed within the framework of the FLOAWER project. This project has received funding from the European Union's Horizon 2020 research and innovation programme under the Marie Sklodowska-Curie grant agreement N° 860879. The authors Vincent Leroy and Erin E. Bachynski-Polić also gratefully acknowledge the West Atlantic Marine Energy Community (WEAMEC), and the financial support from the Pays de la Loire Region, France and Europe (European Regional Development Fund).

References

Abdelmoteleb, S.-E., Mendoza, A.S.E., dos Santos, C.R., Bachynski-Polić, E.E., Griffith, D.T., Oggiano, L., 2022. Preliminary sizing and optimization of semisubmersible substructures for future generation offshore wind turbines. J. Phys.: Conf. Ser. 2362 (1), 012001. http://dx.doi.org/10.1088/1742-6596/2362/1/012001.

Allen, C., Viscelli, A., Dagher, H., Goupee, A., Gaertner, E., Abbas, N., Hall, M., Barter, G., 2020. Definition of the UMaine VolturnUS-S reference platform developed for the IEA Wind 15-Megawatt offshore reference wind turbine. Technical Report NREL/TP-5000-76773, National Renewable Energy Lab.(NREL), Golden, CO (United States).

Arnal, V., 2020. Modélisation expérimentale d'une éolienne flottante par une approche" sofware-in-the-loop". (Ph.D. thesis). Ecole centrale de Nantes.

Campos, A., Molins, C., Trubat, P., Alarcón, D., 2017. A 3D FEM model for floating wind turbines support structures. Energy Procedia 137, 177–185. http://dx.doi.org/10.1016/j.egypro.2017.10.344.

Cheng, Y., Xi, C., Dai, S., Ji, C., Collu, M., Li, M., Yuan, Z., Incecik, A., 2022. Wave energy extraction and hydroelastic response reduction of modular floating breakwaters as array wave energy converters integrated into a very large floating structure. Appl. Energy (ISSN: 0306-2619) 306, 117953. http://dx.doi.org/10.1016/j.apenergy.2021.117953.

Det Norske Veritas, A., 2010. Environmental conditions and environmental loads. DNV-RP-C205.

Faltinsen, O., 1993. Sea Loads on Ships and Offshore Structures, vol. 1. Cambridge University Press.

Gómez, P., Sánchez, G.D., Llana, A., González, G., Berque, J., Aguirre, G., 2015. Oceanographic and meterorological conditions for the design. Technical Report, LIFES50+.

Jonkman, J., 2010. Definition of the Floating System for Phase IV of OC3. Technical Report NREL/TP-500-47535, National Renewable Energy Lab.(NREL), Golden, CO (United States).

Jonkman, J., Branlard, E., Hall, M., Hayman, G., Platt, A., Robertson, A., 2020. Implementation of substructure flexibility and member-level load capabilities for floating offshore wind turbines in OpenFAST. Technical Report, NREL/TP-5000-76822, National Renewable Energy Lab.(NREL), Golden, CO (United States).

Jonkman, J., Musial, W., 2010. Offshore Code Comparison Collaboration (OC3) for IEA Wind Task 23 Offshore Wind Technology and Deployment , vol. 303. Technical Report NREL/TP-5000-48191, National Renewable Energy Lab.(NREL), Golden, CO (United States).

Karimirad, M., Moan, T., 2010. Extreme structural dynamic response of a spar type wind turbine. In: International Conference on Offshore Mechanics and Arctic Engineering, vol. 49118. pp. 303–312.

Karimirad, M., Moan, T., 2011. Extreme dynamic structural response analysis of catenary moored spar wind turbine in harsh environmental conditions. J. Offshore Mech. Arct. Eng. 133 (4).

Karimirad, M., Moan, T., 2012. A simplified method for coupled analysis of floating offshore wind turbines. Marine Struct. 27 (1), 45–63. http://dx.doi.org/10.1016/j.marstruc.2012.03.003.

Leroy, V., Delacroix, S., Merrien, A., Bachynski-Polić, E., Gilloteaux, J.-C., 2022a. Experimental investigation of the hydro-elastic response of a spar-type floating offshore wind turbine. Ocean Eng. 255, 111430. http://dx.doi.org/10.1016/j.oceaneng.2022.111430.

Leroy, V., Delacroix, S., Merrien, A., Bachynski-Polić, E.E., Gilloteaux, J.-C., 2022b. Hydroelastic response of the scaled model of a floating offshore wind turbine platform in waves: HELOFOW Project Database (1.0.0) [data set]. Zenodo. http://dx.doi.org/10.5281/zenodo.8108629.

Li, H., Gao, Z., Bachynski-Polić, E.E., Zhao, Y., Fiskvik, S., 2023. Effect of floater flexibility on global dynamic responses of a 15-MW semi-submersible floating wind turbine. Ocean Eng. 286, 115584. http://dx.doi.org/10.1016/j.oceaneng.2023.115584.

Luan, C., Chabaud, V., Bachynski, E.E., Gao, Z., Moan, T., 2017a. Experimental validation of a time-domain approach for determining sectional loads in a floating wind turbine hull subjected to moderate waves. Energy Procedia 137, 366–381. http://dx.doi.org/10.1016/j.egypro.2017.10.361.

Luan, C., Gao, Z., Moan, T., 2017b. Development and verification of a time-domain approach for determining forces and moments in structural components of floaters with an application to floating wind turbines. Marine Struct. 51, 87–109. http://dx.doi.org/10.1016/j.marstruc.2016.10.002.

Luan, C., Gao, Z., Moan, T., 2018. Comparative analysis of numerically simulated and experimentally measured motions and sectional forces and moments in a floating wind turbine hull structure subjected to combined wind and wave loads. Eng. Struct. 177, 210–233. http://dx.doi.org/10.1016/j.engstruct.2018.08.021.

Robertson, A., Bachynski, E.E., Gueydon, S., Wendt, F., Schünemann, P., 2020. Total experimental uncertainty in hydrodynamic testing of a semisubmersible wind turbine, considering numerical propagation of systematic uncertainty. Ocean Eng. (ISSN: 0029-8018) 195, 106605. http://dx.doi.org/10.1016/j.oceaneng.2019.106605.

Silva de Souza, C.E., Bachynski, E.E., 2020. Effects of hull flexibility on the structural dynamics of a tension leg platform floating wind turbine. J. Offshore Mech. Arct. Eng. 142 (1), http://dx.doi.org/10.1115/1.4044725.

Silva de Souza, C., Bachynski-Polić, E., 2022. Design, structural modeling, control, and performance of 20 MW spar floating wind turbines. Mar. Struct. 84, 103182. http://dx.doi.org/10.1016/j.marstruc.2022.103182.

Thomsen, J., Bergua, R., Jonkman, J., Robertson, A., Mendoza, N., Brown, C., Galinos, C., Stiesdal, H., 2021. Modeling the TetraSpar floating offshore wind turbine foundation as a flexible structure in OrcaFlex and OpenFAST. Energies 14, 7866. http://dx.doi.org/10.3390/en14237866.

Wamit, Inc., 2006. WAMIT User Manual. Chestnut Hill, PA..

Zhao, Z., Wang, W., Shi, W., Qi, S., Li, X., 2022. Effect of floating substructure flexibility of large-volume 10 MW offshore wind turbine semi-submersible platforms on dynamic response. Ocean Eng. (ISSN: 0029-8018) 259, 111934. http://dx.doi.org/10.1016/j.oceaneng.2022.111934.